Check for updates

Synthesis of component-controllable monolayer Mo$_x$W$_{(1-x)}$S$_{2y}$Se$_{2(1-y)}$ alloys with continuously tunable band gap and carrier type†

You Li,[ab] Kangkang Wang, [b] Yiwen Wang,[a] Ziyue Qian,[b] Wenbin Huang,[a] Junqi Wang,[a] Qichao Yang,[a] Honggang Wang,[b] Junyi Liao,[b] Sabir Hussain, [b] Liming Xie [b] and Junjie Qi [*a]

Alloying can effectively modify electronic and optical properties of two-dimensional (2D) transition metal dichalcogenides (TMDs). However, efficient and simple methods to synthesize atomically thin TMD alloys need to be further developed. In this study, we synthesized 25 monolayer Mo$_x$W$_{(1-x)}$S$_{2y}$Se$_{2(1-y)}$ alloys by using a new liquid phase edge epitaxy (LPEE) growth method with high controllability. This straightforward approach can be used to obtain monolayer materials and operates on a self-limiting growth mechanism. The process allows the liquid solution to come into contact with the two-dimensional grains only at their edges, resulting in epitaxy confined only along the in-plane direction, which produces exclusively monolayer epitaxy. By controlling the weight ratio of MoS$_2$/WSe$_2$ (MoSe$_2$/WS$_2$), 25 monolayer Mo$_x$W$_{(1-x)}$S$_{2y}$Se$_{2(1-y)}$ alloys with different atomic ratios can be obtained on sapphire substrates, with band gap ranging from WS$_2$ (1.55 eV) to MoSe$_2$ (1.99 eV) and a continuously broad spectrum ranging from 623 nm to 800 nm. By adjusting the alloy composition, the carrier type and carrier mobility of alloy-based field-effect transistors can be modulated. In particular, the adjustable conductivity of Mo$_x$W$_{(1-x)}$S$_{2y}$Se$_{2(1-y)}$ alloys from n-type to bipolar type is achieved for the first time. This general synthetic strategy provides a foundation for the development of monolayer TMD alloys with multiple components and various 2D materials.

1. Introduction

Unlike zero-bandgap graphene, monolayer transition metal dichalcogenides (TMDs) have a tunable direct bandgap and can be used to fabricate semiconductor devices with excellent performance.[1–10] However, acquiring continuous bandgap tuning is difficult for monolayer TMDs, likely because of certain disadvantages, such as relatively limited variety and uniformity. These drawbacks limit the ability of TMDs to meet diverse electronic and optoelectronic application requirements. Therefore, various strategies have been developed to optimize the energy band structure of TMDs. These methods include doping,[11–14] heterostructure engineering,[15–17] surface functionalization, and alloying.[18–26] Meanwhile, the band gap of 2D TMDs can also be tuned by adjusting the number of layers,[27] as well as by applying stresses and electric fields.[28–32] Among these

approaches, alloying is an easily scalable technique that can be used to design energy band structures.

Ternary monolayer TMD alloys such as WS$_{2x}$Se$_{2(1-x)}$, MoS$_{2(1-x)}$Se$_{2x}$, and ReS$_{2x}$Se$_{2(1-x)}$ have exhibited versatile optical and electronic properties.[33–36] By tuning the ratio of S to Se,[23] the direct band gap of the monolayer MoS$_{2(1-x)}$Se$_{2x}$ alloy can be tuned completely from pure MoSe$_2$ ($x = 1$, $E_g = 1.56$ eV) to pure MoS$_2$ ($x = 0$, $E_g = 1.86$ eV). Alloying also allows for the structural and phase transformation of monolayer TMDs (*e.g.*, rapid phase control from 1H to DT in single-molecule layer W$_{1-x}$Re$_x$S$_2$ alloys by adjusting the ratio of Re/W).[26] In addition, monolayer TMD alloys have lower free and internal energies, resulting in improved thermal stability. Various synthesis techniques have been developed to obtain high-quality monolayer TMD alloys. Xie *et al.* prepared monolayer MoS$_{2(1-x)}$Se$_{2x}$ materials with multiple components by physical vapor deposition (PVD).[37] Xiang *et al.* fabricated high-quality monolayer WS$_{2(1-x)}$Se$_{2x}$ materials with tunable forbidden bandgap widths by chemical vapor deposition (CVD) on SiO$_2$/Si substrates.[34] Using a sodium chloride-assisted confined-space CVD method, Xiao *et al.* synthesized large-size monolayer WeS$_{2(1-x)}$Se$_{2x}$ films on SiO$_2$/Si substrates.[38] The aforementioned strategies show potential for growing high-quality TMD alloys, but these synthesis techniques are uncontrollable and complicated. For instance, the

[a]*School of Materials Science and Engineering, University of Science and Technology Beijing, Beijing 100083, P. R. China. E-mail: junjieqi@ustb.edu.cn*

[b]*CAS Key Laboratory of Standardization and Measurement for Nanotechnology, National Center for Nanoscience and Technology, Beijing 100190, China*

† Electronic supplementary information (ESI) available. See DOI: https://doi.org/10.1039/d3ra07065d

PVD method requires good stability and easy sublimation of the precursor at the growth temperature, so the growth temperature and precursor are critical parameters in the TMD alloys growth process, and unsuitability of either parameter can produce by-products. In conventional CVD, the precursor vapor pressure determines the growth directly. The vapor pressure in CVD is closely associated with the reaction temperature and the precursor-substrate distance, and minor variations in these two parameters may induce sharp vapor pressure fluctuations, leading to the generation of undesired by-products during the synthesis process of TMD alloys. Meanwhile, confined-space CVD method is complicated by the requirement of a suitable confinement strategy to be designed. Moreover, studies on the synthesis of TMD alloys have mostly focused on ternary TMD alloys and rarely on quaternary TMD alloys. The synthesis of high-quality tunable quaternary monolayer TMD alloys continues to present a significant challenge.

According to the liquid phase edge epitaxy (LPEE) growth mechanism previously proposed by our research group,[39] 25 monolayer $Mo_xW_{(1-x)}S_{2y}Se_{2(1-y)}$ alloys with different atomic ratios can be obtained on sapphire substrates. In LPEE, the solution only contacts the edges of the two-dimensional grains, restricting epitaxy in the in-plane direction. Consequently, monolayer alloys are formed. By adjusting the weight ratio of MoS_2 and WSe_2 ($MoSe_2$ and WS_2) powders, $Mo_xW_{(1-x)}S_{2y}Se_{2(1-y)}$ monolayer alloys with different atomic ratios can be obtained, and the bandgap of the as-grown alloys can be continuously adjusted from WS_2 (1.55 eV) to $MoSe_2$ (1.99 eV). Due to the adjustable bandgap, quaternary TMD alloys have a wide range of applications in the fields of switching devices, radio frequency (RF) devices, optoelectronic devices, and so on. This LPEE method is applicable for the preparation of high-quality and controllable quaternary monolayer TMD alloys with precise tunability of composition. The atomic ratio of each component in the $Mo_xW_{(1-x)}S_{2y}Se_{2(1-y)}$ alloys was calculated using X-ray photoelectron spectroscopy (XPS). Variations in the electronic bandgap of 25 quaternary TMD alloys with different component ratios were measured using photoluminescence (PL). The complex structural arrangement of monolayer $Mo_xW_{(1-x)}S_{2y}Se_{2(1-y)}$ was investigated using scanning transmission electron microscopy (STEM). By adjusting alloys composition, carrier type and carrier mobility of alloy-based field-effect transistors can be modulated. In particular, the adjustable conductivity of $Mo_xW_{(1-x)}S_{2y}Se_{2(1-y)}$ alloys from n-type to bipolar type is achieved.

2. Experimental

2.1. Material growth

Monolayer $Mo_xW_{(1-x)}S_{2y}Se_{2(1-y)}$ were obtained in a single-temperature zone CVD tube furnace (Fig. S1†). $MoSe_2$ (MoS_2) powder (99.99%, Macklin) and WS_2 (WSe_2) powder (99.99%, Macklin) in different mass ratios were mixed (total weight = 0.05 g) and then placed inside the quartz boat, together with 1 g of NaCl powder (99.5%, Macklin) as precursors. Sapphire wafers ($\sim$10 × 18 mm^2) as substrates were treated with a mixture consisting of acetone, ethanol, and isopropanol. They were then

placed upside down on a quartz vessel at the center of the furnace. Prior to heating, the system was vacuum-pumped for 15 min and flushed with 500 sccm Ar (99.999% purity) gas to remove air. Pumping was subsequently discontinued to allow the pressure in the system to return to atmospheric pressure. The furnace temperature was raised to the growth temperature (900 °C) within 30 min and maintained for 1 h. During the growth, 10 sccm Ar gas was used as the carrier gas. After the heating was discontinued, the furnace temperature was allowed to decrease to 500 °C before the chamber door was opened. The chamber was allowed to rapidly cool down to room temperature. The alloys were removed from the chamber. The surfaces were gently washed with deionized water to remove the extra salt and then blown dry with nitrogen gas for preservation.

2.2. Preparation and characterization of TEM/STEM samples

The monolayer as-grown samples were transferred onto Cu grids *via* a wet polymethyl methacrylate (PMMA) transfer method. A PMMA layer (3000 rpm for 60 s) was spin-coated on the substrate with deposited samples. This operation was performed thrice. Substrate was then baked at 120 °C for 20 min. The $PMMA/Mo_xW_{(1-x)}S_{2y}Se_{2(1-y)}$ film on the sapphire was then transferred onto a Cu grid by using tape. It was then soaked in acetone for 40 min at 60 °C until the PMMA was removed. Finally, the copper grid was washed with isopropanol and subsequently removed from it until it was dry.

TEM and STEM images, selected area electron diffraction (SAED) mode, and energy-dispersive spectroscopy (EDS) maps were acquired on a JEM-F200 (JEOL) unit operating at 200 kV. The high-angle annular dark-field scanning transmission electron microscopy (HAADF-STEM) images were recorded using a transmission electron microscope with a double Cs-corrected JEM-ARM200CF (JEOL) operated at 80 kV, equipped with a CEOS Cs corrector (CEOS GmbH, Heidelberg, Germany).

2.3. Raman and photoluminescence spectroscopy

Raman/PL characterization was conducted using a Raman microscope (Renishaw inVia) with a laser wavelength of 532 nm, power of 10%, and PL power of 1%. Raman maps were set in steps of 0.5 μm. Image processing was performed using the software Renishaw Wire 4.2.

2.4. DFT calculation

Density functional theory (DFT) simulation was conducted by Vienna *Ab initio* Simulation Package (VASP) software with the projector augmented wave (PAW) method. The convergence value of energy was set as 10^{-5} eV, and the convergence value of force on each atom was 0.05 eV Å^{-1}. Hubbard-U correction was added.

2.5. Characterization of morphology and composition

Optical images of monolayer $Mo_xW_{(1-x)}S_{2y}Se_{2(1-y)}$ alloys were captured by optical microscopy (OM, Olympus, BX51) and atomic force microscopy (AFM, Bruker, Dimension Icon). X-ray photoelectron spectroscopy (XPS) spectra were acquired using

the ESCALAB 250Xi (ThermoFisher Scientific, UK) and 200 eV X-rays (Al K-alpha). XPS peaks were analyzed and fitted using the software Advantage and Original.

2.6. Device fabrication and measurement

The mask was utilized to pattern the source and drain. Cr/Au electrodes were deposited with thickness of 10/60 nm by electron beam evaporation system. Electrical transport measurements of alloy FETs under vacuum were conducted by a Keithley 4200-SCS semiconductor analyzer.

3. Result and discussion

As shown in Fig. 1a, the atomic scheme for the nucleation and growth procedure in LPEE comprises eutectic melting, nucleation and growth, and the remaining monolayer TMD alloys. In Stage 1, the molten salt (solvent) and TMD precursors (solute) melted above the eutectic melting point temperature. At elevated vapor pressure and temperature, partial evaporation of the molten salt led to the supersaturation of the solution. Consequently, the monolayer TMD alloys began to nucleate and crystallize (Stage 2). The growth of the alloy flakes was driven by the motion of the droplets, which only touched the edges of the alloy flakes. This limited contact physically prevented the nucleation and growth of alloy flakes and inhibited the growth of alloy flakes with few layers. Finally, most of the molten salt evaporated and the monolayer TMD alloys remained on the substrate (Stage 3).

As shown in Fig. 1d, the quaternary $Mo_{0.82}W_{0.18}S_{0.28}Se_{1.72}$ is successfully synthesized using LPEE. The synthesized $Mo_{0.82}W_{0.18}S_{0.28}Se_{1.72}$ alloy is monolayer with regular triangular morphologies, and other quaternary alloys with irregular shapes may be attributed to the competition of different boundary free energies, which determine the growth rate of each edge, ultimately affecting the morphological structure.[8] The quaternary $Mo_{0.82}W_{0.18}S_{0.28}Se_{1.72}$ alloy was confirmed as
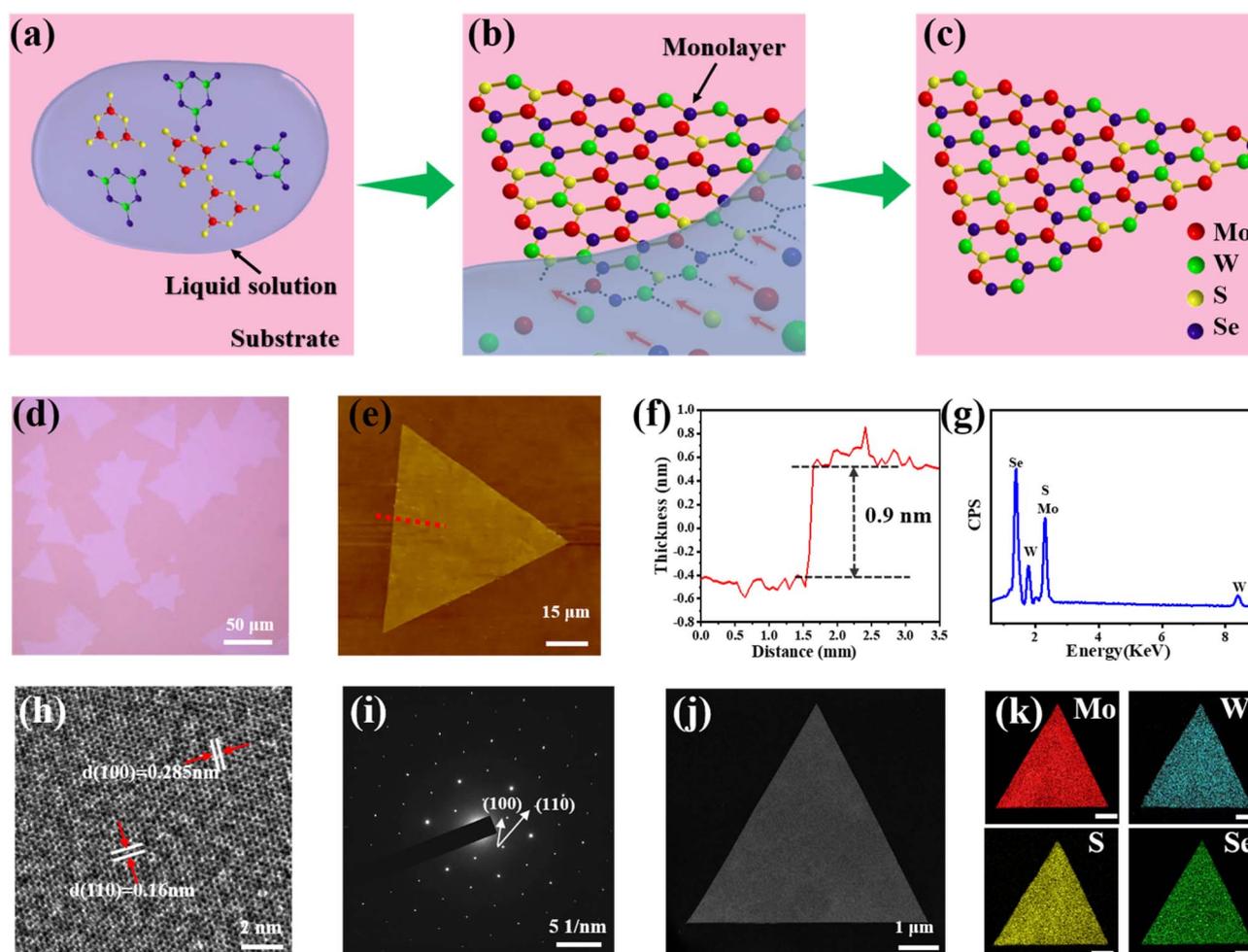

Fig. 1 Synthesis of monolayer $Mo_xW_{(1-x)}S_{2y}Se_{2(1-y)}$ by LPEE. (a)–(c) Schematic of the nucleation and growth of $Mo_xW_{(1-x)}S_{2y}Se_{2(1-y)}$. (d) OM image of $Mo_{0.82}W_{0.18}S_{0.28}Se_{1.72}$ on the sapphire substrate. (e) AFM image of $Mo_{0.82}W_{0.18}S_{0.28}Se_{1.72}$. (f) Height profile (along the red dashed line) in the AFM images of $Mo_{0.82}W_{0.18}S_{0.28}Se_{1.72}$. (g) EDS elemental analysis of $Mo_{0.82}W_{0.18}S_{0.28}Se_{1.72}$. (h) HRTEM image of $Mo_{0.82}W_{0.18}S_{0.28}Se_{1.72}$. (i) SAED image of $Mo_{0.82}W_{0.18}S_{0.28}Se_{1.72}$. (j) STEM image of $Mo_{0.82}W_{0.18}S_{0.28}Se_{1.72}$ on Cu grids. (k) EDS mapping images of the elements Mo, W, S, and Se in $Mo_{0.82}W_{0.18}S_{0.28}Se_{1.72}$. Scale bar: 1 μm.

monolayer structures by AFM. Fig. 1e and f presents the AFM images and height profiles of the isolated flakes, the heights of the flakes are about 0.9 nm, which is consistent with the height of a monolayer alloy.[40–42] These flakes have a smooth flat surface with uniform thickness and no cracks.

To evaluate the crystallinity of the grown monolayer Mo_x-$W_{(1-x)}S_{2y}Se_{2(1-y)}$ obtained using the proposed LPEE method, we selected the monolayer $Mo_{0.82}W_{0.18}S_{0.28}Se_{1.72}$ as representative for electron microscopy characterization. During the wet transfer process, we used PMMA as a transfer film to move the grown alloys from the sapphire substrate to the Cu grids for TEM characterization. As shown in Fig. 1h, the HRTEM image of the monolayer $Mo_{0.82}W_{0.18}S_{0.28}Se_{1.72}$ shows a honeycomb structure exhibiting a clear hexagonal atomic arrangement, with a spacing of about 0.16 nm in the (110) crystal plane

direction and 0.285 nm in the (100) crystal plane. As shown in Fig. 1i, SAED shows 6 identical diffraction spots, indicating the single crystal nature and good crystallinity of the monolayer $Mo_{0.82}W_{0.18}S_{0.28}Se_{1.72}$.[43–47] Fig. 1k presents the EDS mapping images, and the corresponding EDS spectra are shown in Fig. 1g, which reveals the uniform distribution of Mo, W, S, and Se in the alloy.

Raman spectroscopy was conducted to analyze the structural composition of the synthesized quaternary monolayer Mo_x-$W_{(1-x)}S_{2y}Se_{2(1-y)}$. The Raman spectra of $Mo_xW_{(1-x)}S_{2y}Se_{2(1-y)}$ synthesized with different weight ratios of MoS_2 and WSe_2 powders reveal two different in-plane vibrational peaks in the spectrum (Fig. 2a), caused by the E_{2g}^1 vibrational modes of the Mo–S and W–S bonds, respectively.[23,24] As the MoS_2 content increased, the E_{2g}^1 mode peak of WS_2 produces a blueshift,
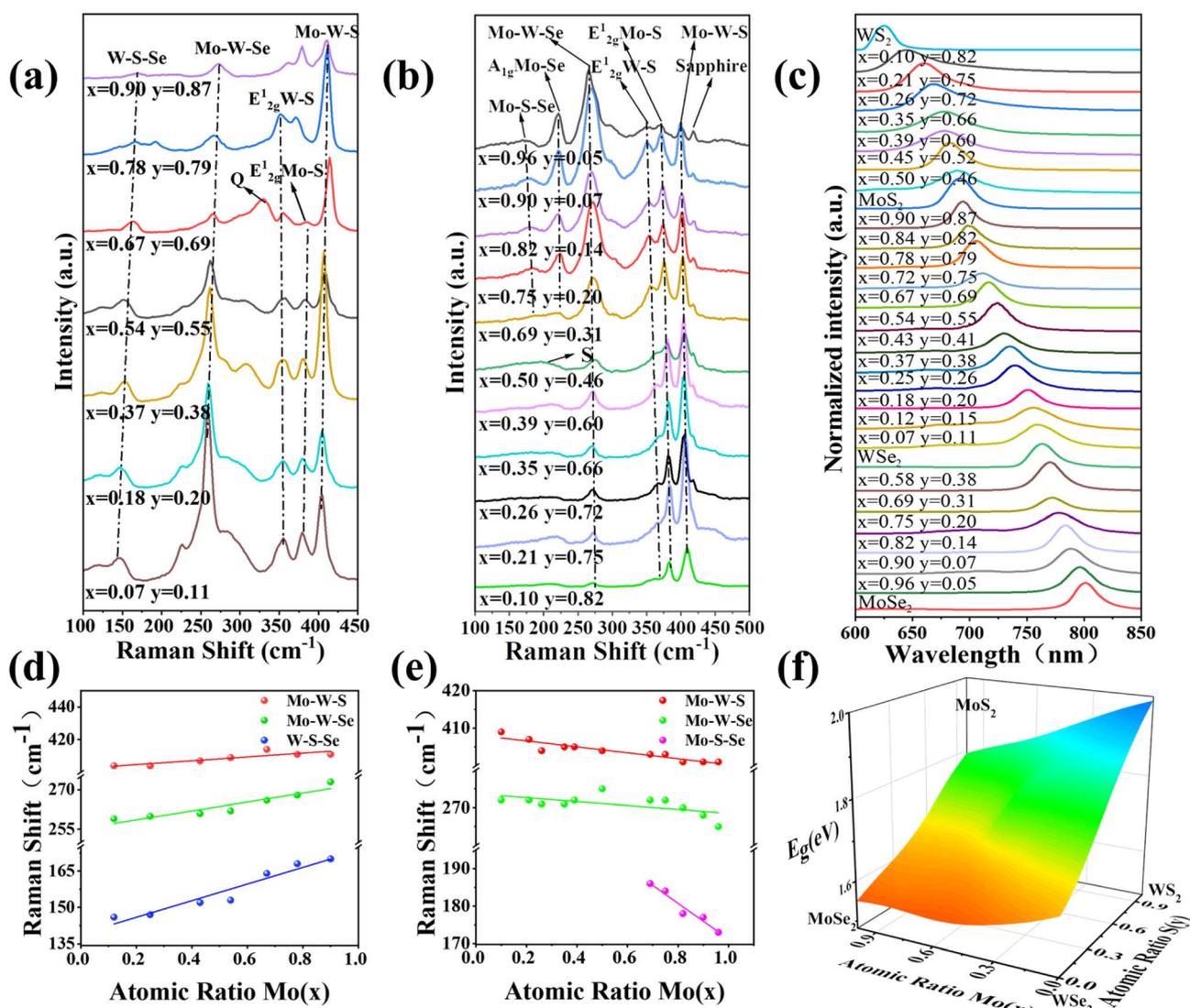

Fig. 2 Raman and PL studies of monolayer $Mo_xW_{(1-x)}S_{2y}Se_{2(1-y)}$ with different ratios. (a) Raman spectra of $Mo_xW_{(1-x)}S_{2y}Se_{2(1-y)}$ with different weight ratios of MoS_2 and WSe_2 as growth sources. (b) Raman spectra of $Mo_xW_{(1-x)}S_{2y}Se_{2(1-y)}$ alloys with different weight ratios of $MoSe_2$ and WS_2 as growth sources. (c) Normalized PL spectra of $Mo_xW_{(1-x)}S_{2y}Se_{2(1-y)}$. (d) Composition-dependent Raman frequencies of $Mo_xW_{(1-x)}S_{2y}Se_{2(1-y)}$ with different weight ratios of MoS_2 and WSe_2 as growth sources. (e) Composition-dependent Raman frequencies of $Mo_xW_{(1-x)}S_{2y}Se_{2(1-y)}$ with different weight ratios of $MoSe_2$ and WS_2 as growth sources. (f) 3D band bowing diagram of $Mo_xW_{(1-x)}S_{2y}Se_{2(1-y)}$.

whereas the E_{2g}^1 mode peak of MoS_2 produces a redshift. Three major peaks are also observed. The first peak at the low frequency can be attributed to the (E_{2g}(S–W) – LA(S–W) + A_{1g}(Se–W) – LA(Se–W)) W–S–Se bond vibration, with LA denoting the longitudinal acoustic mode.[25] The second peak corresponds to the Mo–W–Se bond vibration. The third peak is the Mo–W–S bond vibration attributed to the combined A_{1g} peak of Mo–S and W–S. We further observed that when x is 0.67 and y is 0.69, the alloy showed a Q-peak (330 cm^{-1}). This Q-peak is resulted from mixing of Mo, W, S and Se has been named as quaternary peak. The vibration mode of this peak position is yet to be explored.[25] Fig. 2d and S3† show the composition-dependent Raman frequencies of $Mo_xW_{(1-x)}S_{2y}Se_{2(1-y)}$. As the atomic ratio x (y) changes from 0.24 (1.42) to 0.95 (1.68), the low-frequency W–S–Se continuously shifts from 146 cm^{-1} to 168 cm^{-1}, the high-frequency Mo–W–Se continuously shifts from 259 cm^{-1} to 273 cm^{-1}, and the higher-frequency Mo–W–Se continuously shifts from 404 cm^{-1} to 411 cm^{-1}. The Raman peaks shift because some Mo and S atoms of the original monomolecular layer are replaced by Se and W atoms. Mo and W atoms have similar atomic radii, but Se atoms have a larger atomic radius than S atoms in the same group. Therefore, the addition of Se atoms alters the symmetry of MoS_2 crystals, generates tensile strain in the lattice, and modifies the original chemical bonds.[33] With an increase in the proportion of Se atoms, the chemical bonds associated with Se atoms change, causing a shift in the Raman peak position, which is consistent with the literature.[23,34]

Different mass ratios of $MoSe_2$ and WS_2 powders were selected as the growth source and were varied to synthesize $Mo_xW_{(1-x)}S_{2y}Se_{2(1-y)}$, thus ensuring the integrity of the experiment. Fig. 2b presents the relevant Raman spectra. The characteristic peak of the out-of-plane vibrational $MoSe_2$-like A_{1g} mode appears at 221 cm^{-1}, whereas the characteristic peak belonging to the Mo–S–Se bond vibrational mode appears in the low-frequency region. The observations contradict the results when the growth sources are MoS_2 and WSe_2. This finding suggests that the S atoms tend to bond with Mo, Se atoms in the Se-rich environment, and the peak of the Mo–S–Se bond blueshift as the $MoSe_2$/WS_2 mass ratio decreases. When x is less than 0.50 and y is less than 0.46, the peak from the Mo–S–Se bond vibrational mode merges with the peak from the $MoSe_2$-like A_{1g} mode into a single peak (S) of reduced intensity. To clarify these results, we determined the trend of the Raman peak frequencies by linear fitting. The characteristic peaks identified in Fig. 2e and S3† vary consistently. Specifically, as the atomic ratio Mo (x) or Se ($1-y$) decrease, the peak corresponding to the Mo–S–Se blueshifts from 173 cm^{-1} to 186 cm^{-1} and then disappears. Similarly, the peak of the Mo–W–Se blueshifts from 265.3 cm^{-1} to 272 cm^{-1}, and the peak
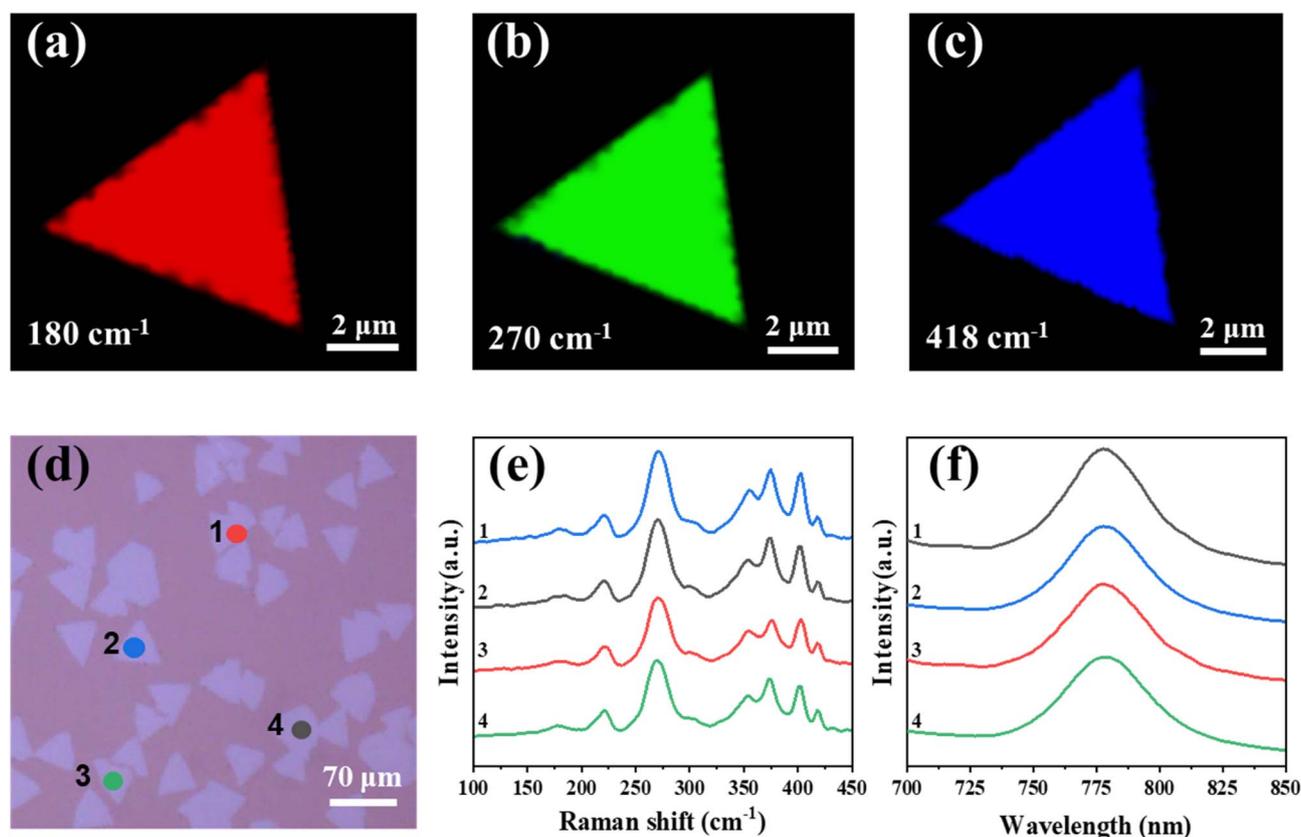

Fig. 3 Homogeneity characterization of the monolayer $Mo_xW_{(1-x)}S_{2y}Se_{2(1-y)}$. (a–c) Raman (180 cm^{-1}, 270 cm^{-1}, 418 cm^{-1}) intensity mappings of monolayer $Mo_{0.82}W_{0.18}S_{0.28}Se_{1.72}$ alloy. (d) Typical OM image of monolayer $Mo_{0.82}W_{0.18}S_{0.28}Se_{1.72}$ alloy on sapphire substrate. (e and f) The corresponding Raman and PL spectra at four points measured from the substrate in (a).

© 2023 The Author(s). Published by the Royal Society of Chemistry

corresponding to Mo–W–S blueshifts from 400.2 cm^{-1} to 407.5 cm^{-1}. The shifts of the aforementioned Raman peaks are also primarily attributed to the mixed crystal disorder effect.[34]

PL tests were performed at room temperature to evaluate the optical properties of 25 different atomic ratios of the monolayer $Mo_xW_{(1-x)}S_{2y}Se_{2(1-y)}$ and 4 pure TMDs. The normalized PL spectra of the 25 different atomic ratios of monolayer TMD alloys and 4 pure TMDs show that all spectra have a single emission peak and no defects or structurally disturbed peaks at lower energies exist, indicating the high quality of the lamellar crystals (Fig. 2c). As the atomic ratio Mo (x) and S (y) changes, the position of the PL single peak continuously blueshifts from 1.99 eV (623 nm) to 1.55 eV (800 nm). The results clarify that the band gaps of quaternary alloys can be adjusted substantially within a range bounded by the band gaps of $MoSe_2$ and WS_2 by varying the weight ratio of the growth source. Changes in the trends of band gaps can be described more intuitively. Fig. 2f shows the 3D band bowing diagram of the monolayer $Mo_xW_{(1-x)}S_{2y}Se_{2(1-y)}$. The peak position of the alloy exhibits a nonlinear variation with the atomic ratio Mo (x) or S (y). This nonlinear peak variation is also called a "bowing effect" and has also been reported in other 2D TMD alloys,[23,24,34] mainly attributed to crystal mismatch.

To investigate the homogeneity of the as-grown monolayer $Mo_xW_{(1-x)}S_{2y}Se_{2(1-y)}$, we performed Raman mapping characterization of the monolayer $Mo_{0.82}W_{0.18}S_{0.28}Se_{1.72}$ (Fig. 3a–c). The corresponding variation intensities at frequencies of 179 cm^{-1} (red), 270 cm^{-1} (green), and 404 cm^{-1} (blue) are Mo–S–Se, Mo–W–Se, and Mo–W–S, respectively. The consistency of the intensity confirms the homogeneous distribution of the component and stress in the isolated triangular flake, further indicating the uniform distribution of Mo, W, S, and Se in the lattice of the monolayer $Mo_xW_{(1-x)}S_{2y}Se_{2(1-y)}$. In addition, we recorded randomly selected Raman and PL spectra at four different alloy TMD domains from 1 to 4 in the substrate (Fig. 3d). The Raman and PL peaks at different domains on sapphire substrate are almost identical, which is highly indicative of their thickness and compositional consistency of as-grown monolayer $Mo_xW_{(1-x)}S_{2y}Se_{2(1-y)}$ on sapphire substrate (Fig. 3e and f).

To further study the PL characteristics of the as-grown sample with different atomic ratios, we used the density functional theory (DFT) and the Vienna *Ab Initio* Simulation Package,[48] together with the projector augmented wave (PAW)[49] method, to evaluate variations in the energy band gap. Fig. 4a–c present the top and side views of the atomic structures of 3 monolayer $Mo_xW_{(1-x)}S_{2y}Se_{2(1-y)}$ with different atomic ratios. TMDs such as 2H-MX$_2$ (M = Mo, W; X = S, Se) are perfect hexagonal symmetric structure crystals; thus, the mutual doping of two TMDs only slightly affects the respective intrinsic

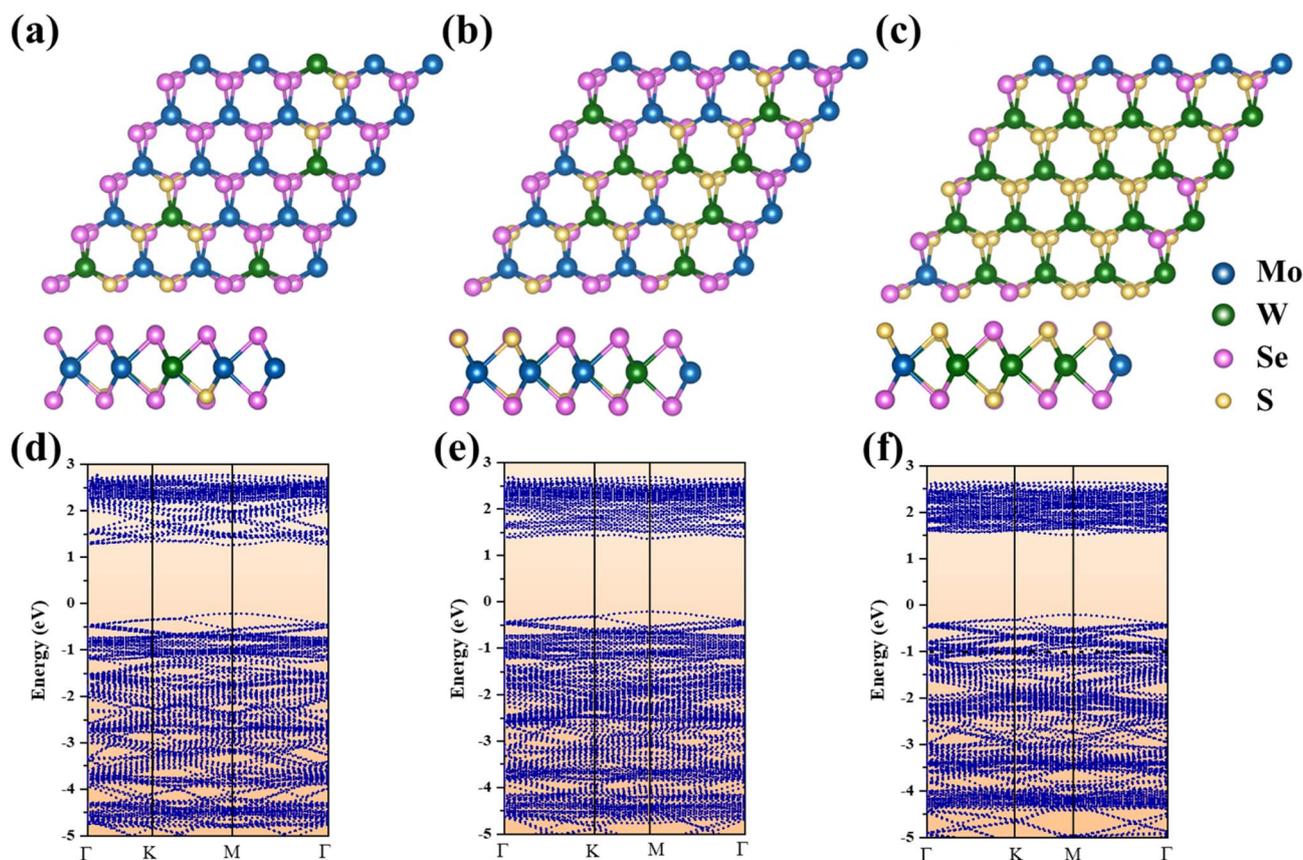**Fig. 4** DFT calculations of the monolayer $Mo_xW_{(1-x)}S_{2y}Se_{2(1-y)}$. Optimized top and side view structures of (a) $Mo_{0.82}W_{0.18}S_{0.28}Se_{1.72}$, (b) $Mo_{0.69}W_{0.31}S_{0.62}Se_{1.38}$, (c) $Mo_{0.26}W_{0.74}S_{1.44}Se_{0.56}$. (Mo, blue; W, green; S, yellow; Se, pink). Band structure of (d) $Mo_{0.82}W_{0.18}S_{0.28}Se_{1.72}$, (e) $Mo_{0.69}W_{0.31}S_{0.62}Se_{1.38}$, (f) $Mo_{0.26}W_{0.74}S_{1.44}Se_{0.56}$.

hexagonal lattice structure. Consequently, the structure of as-grown alloys remains hexagonal. Fig. 4d–f show the energy band structure diagrams of 3 monolayer $Mo_xW_{(1-x)}S_{2y}Se_{2(1-y)}$ with different composition. According to DFT calculations, all structures exhibit a direct band gap and the band gap values are 1.57, 1.62, and 1.72 eV, respectively, slightly lower than the experimental values (1.58, 1.66 and 1.80 eV). Meanwhile with increasing W and S atomic ratios, the calculated band gap of $Mo_xW_{(1-x)}S_{2y}Se_{2(1-y)}$ continues to increase, which trend is consistent with the experimental results.[34,49]

To elucidate the optical properties, we selected the monolayer $Mo_{0.82}W_{0.18}S_{0.28}Se_{1.72}$ for low-temperature PL measurements (Fig. 5a). Such measurements not only yield the dependence of the band gap on temperature but also help identify the physical mechanisms controlling photoemission. As shown in Fig. 5a, at 300 K, the PL intensity of the monolayer $Mo_{0.82}W_{0.18}S_{0.28}Se_{1.72}$ decreases significantly relative to that at low temperatures. Generally, the luminescence peak of the alloy widens, and the luminescence intensity decreases as the temperature increases (Fig. 5b). This behavior is due to the exponential enhancement of the nonradiative electron–hole complexation process, which reduces the probability of a radiative transition. As shown in Fig. 5a and c, as temperature increases, the PL peak position is red-shifted, which is typically observed in most semiconductor materials.[27] This shift primarily results from dynamic electron–phonon interactions; meanwhile, the role of static lattice expansion is considerably smaller.

The composition and chemical state of the monolayer Mo_x-$W_{(1-x)}S_{2y}Se_{2(1-y)}$ were further analyzed by XPS. The Mo 3d, W 4f, S 2p, and Se 3d signals were fitted by splitting the peaks. Splitting the energy levels by spin–orbit coupling also lead to the splitting of the 3d peaks of the Mo^{4+} oxidation state to form $3d_{3/2}$ and $3d_{5/2}$ peaks at 233.1 and 230.3 eV, separately (Fig. 5d). The W 4f peak corresponding to the W^{4+} oxidation state split into $4f_{5/2}$ (35.1 eV) and $4f_{7/2}$ (32.8 eV) (Fig. 5e). The two
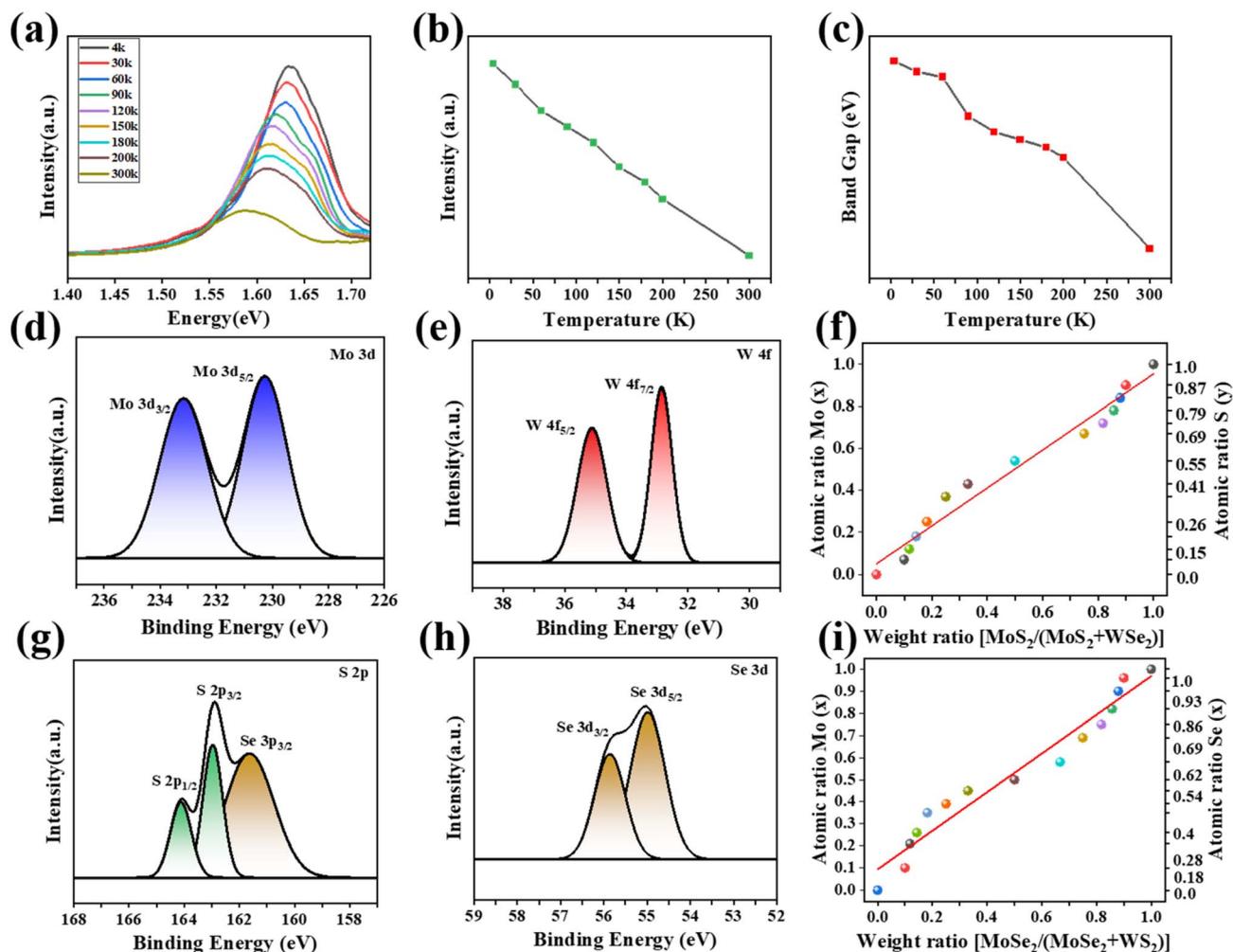

Fig. 5 Characterization of the monolayer $Mo_xW_{(1-x)}S_{2y}Se_{2(1-y)}$. (a) Temperature-dependent PL spectrum of $Mo_{0.82}W_{0.18}S_{0.28}Se_{1.72}$. (b) Temperature-dependent PL intensity variation plot of $Mo_{0.82}W_{0.18}S_{0.28}Se_{1.72}$. (c) Temperature-dependent band gap (PL peak energy) variation plot of $Mo_{0.82}W_{0.18}S_{0.28}Se_{1.72}$. (d–g) XPS spectra of Mo 3d, W 4f, S 2p, and Se 3d core-level binding energies of $Mo_xW_{(1-x)}S_{2y}Se_{2(1-y)}$. (h) Plot of Mo(S) content obtained by XPS *versus* weight ratios of $MoS_2/(MoS_2 + WSe_2)$ applied for the prepared $Mo_xW_{(1-x)}S_{2y}Se_{2(1-y)}$. (i) Plot of Mo (Se) content obtained by XPS *versus* weight ratios of $MoSe_2/(MoSe_2 + WS_2)$ applied for prepared $Mo_xW_{(1-x)}S_{2y}Se_{2(1-y)}$.

characteristic peaks of S^{2-} are located at $2p_{1/2}$ (164.1 eV) and $2p_{3/2}$ (162.9 eV) (Fig. 5g). In addition, Se $3p_{3/2}$ peaks that overlapping with the S 2p region are observed in the S 2p spectrum. Two characteristic peaks are located at $3d_{3/2}$ (56.1 eV) and $3d_{5/2}$ (55.2 eV) in Se, attributed to the Se^{2-} state (Fig. 5h). We quantified the atomic composition of the alloy by employing the software Advantage 4.2 (Fig. S4–S7 and Table S1, S2†). The atomic ratios of Mo (x) and S (y) in the alloy linearly decrease as the weight ratio of $MoS_2/(MoS_2 + WSe_2)$ is reduced from 0.9 to 0.1 (Fig. 5f). When MoS_2 and WSe_2 were selected as the growth sources, the pattern of change is almost consistent (Fig. 5i).

To further investigate the sophisticated atomic distribution in the monolayer $Mo_xW_{(1-x)}S_{2y}Se_{2(1-y)}$, we also examined the monolayer $Mo_{0.82}W_{0.18}S_{0.28}Se_{1.72}$ by using STEM. In Fig. 6a, the Mo, W sites and the sites of the 2 chalcogenides can be clearly distinguished. To assess the distribution of each atom in the quaternary alloy, we conducted a statistical analysis on a STEM image with dimension of 15×15 nm^2. First, the types of atoms in the STEM image are distinguished into metal (M) sites and chalcogenide (X_2) sites on the basis of intensity and coordination relationships. As shown in Fig. 6b, based on the Z-contrast nature of the STEM image,[33,35,47] the intensity histograms of all M sites show two peaks, which are classified as "Mo site" and "W site" regions and denoted by yellow and red. The intensities of the X_2 site are shown in Fig. 6c. Similarly, the intensity histograms of all X_2 sites reveal three peaks classified as the "SS site," "SSe site," and "SeSe site" regions and denoted by green, cyan, and blue, respectively. The distributions of Mo, W, S, and Se are quantified in the 15×15 nm^2 STEM image. The overall statistical results indicate that 532 SS sites, 850 SSe sites, and 3113 SeSe sites are identified from a total of 4495 X_2 sites. The probability of a X_2 site being a "SeSe site" (represented as $P(SeSe)$) is $3113/(532 + 850 + 3113) = 0.693$. Similarly, the probabilities of a "SS site" and a "SeSe site," expressed as $P(SS)$ and $P(SSe)$, are 0.118 and 0.189, respectively. Assuming that SS and SSe are randomly distributed in X_2 sites, the total probabilities of $P(SS)$ and $P(SSe)$ also holds for each X_2 site. Therefore, the probability of each site distribution can be calculated using the binomial distribution. With the calculation of the SSe site as an example,[50]

$$f(k; N, P(SSe)) = \frac{N!}{k!(N-k)!} P(SSe)^k (1 - P(SSe))^{N-k} \quad (1)$$

where N is the total number of X_2 sites in the region, and k is the number of SSe sites in the region. The same analysis applies to the M site. To test this random distribution hypothesis, we cut the entire image into identical 25×25 parts. The statistical histograms of the "site" of these 625 parts are shown in Fig. 6d, e and S6, S7,† which match well with the dashed lines calculated by the binomial distribution. This finding clearly demonstrates the random distribution of Mo, W, S, and Se atoms in quaternary TMD alloys.

To further investigate the quality and composition dependence of monolayer alloys, back-gate field effect transistors (FETs) were fabricated using different component alloys on SiO_2/Si substrates. Fig. 7a shows the schematic diagram of the FET. Fig. 7b demonstrates the Optical images of $Mo_{0.84}W_{0.16}S_{1.64}Se_{0.36}$ and $Mo_{0.18}W_{0.72}S_{0.40}Se_{1.60}$ FETs.
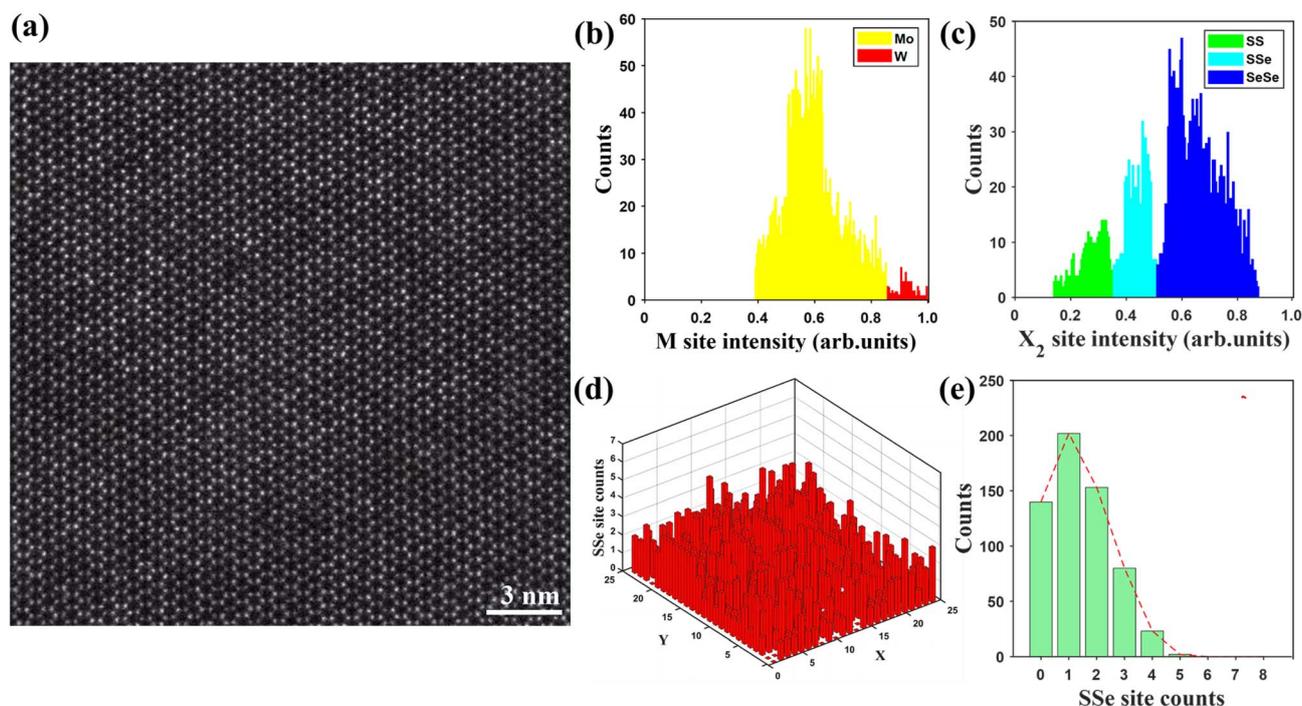

Fig. 6 STEM analysis of the monolayer $Mo_xW_{(1-x)}S_{2y}Se_{2(1-y)}$. (a) HAADF-STEM atomic image of $Mo_{0.82}W_{0.18}S_{0.28}Se_{1.72}$. Scale bar: 3 nm. (b and c) Histograms of HAADF intensity for metal (M) and chalcogenide (X_2) sites in (a), separately. (d) SSe-site distribution histograms in (a). Image was divided into 25×25 parts. (e) Corresponding statistical histogram of SSe-site counts in each part of (a).
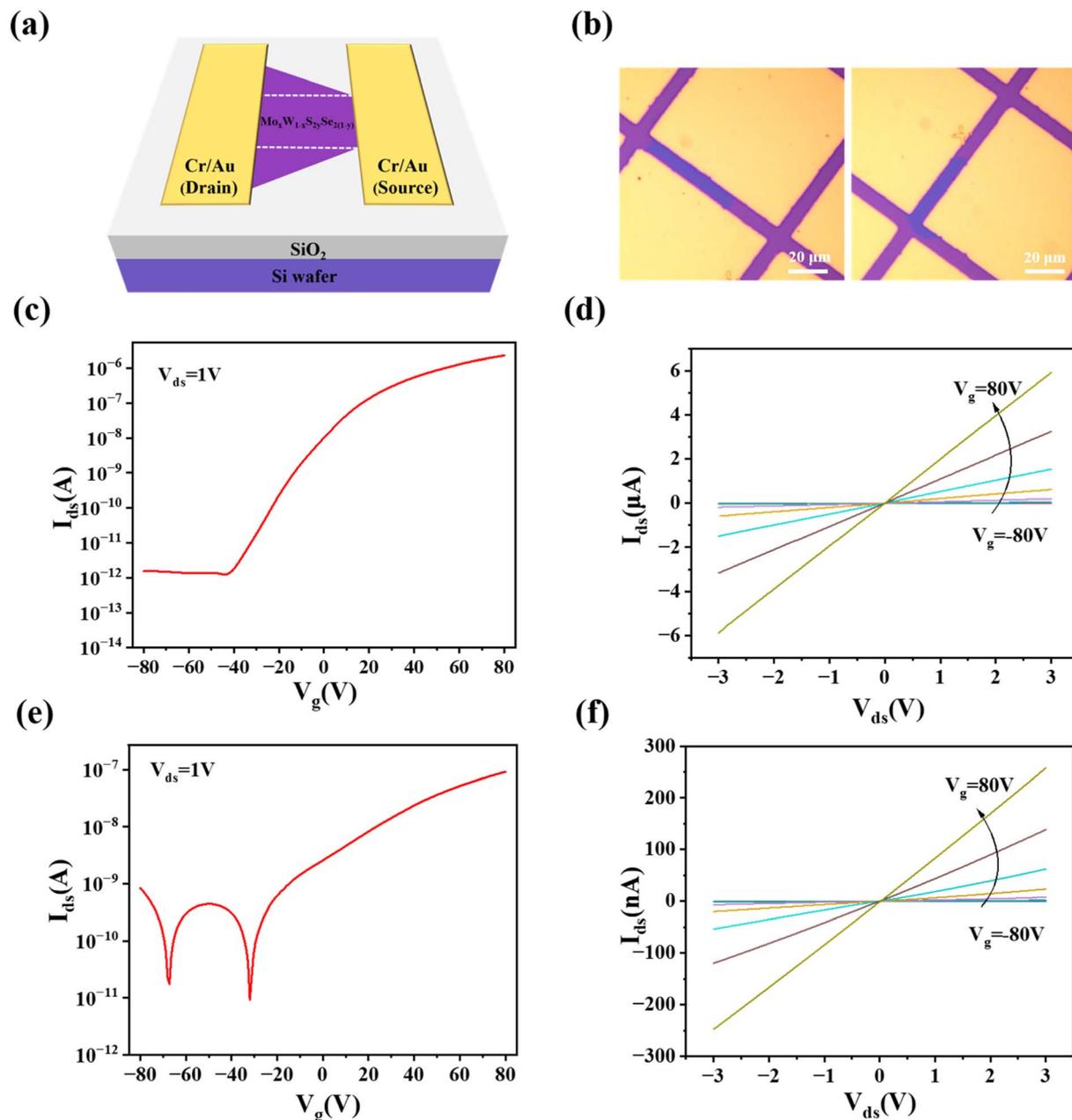
Fig. 7 Electrical measurement of monolayer $Mo_xW_{(1-x)}S_{2y}Se_{2(1-y)}$. (a) Schematic diagram of a monolayer $Mo_xW_{1-x}S_{2y}Se_{2(1-y)}$ FET. (b) Optical image of prepared FETs. (c) Transfer curve of a monolayer $Mo_{0.84}W_{0.16}S_{1.64}Se_{0.36}$-based FET. (d) Output curve of a monolayer $Mo_{0.84}W_{0.16}$-$S_{1.64}Se_{0.36}$-based FET. (e) Transfer curve of a monolayer $Mo_{0.18}W_{0.72}S_{0.40}Se_{1.60}$-based FET. (f) Output curve of a monolayer $Mo_{0.18}W_{0.72}S_{0.40}$-$Se_{1.60}$-based FET.

The transfer curves of the monolayer $Mo_{0.84}W_{0.16}S_{1.64}Se_{0.36}$ alloy FET measured at room temperature, demonstrating the n-type semiconductor transfer behavior and on/off current ratio obtained is about 10^6 (Fig. 7c). We can calculate the carrier mobility from the transfer ($I_{ds} - V_g$) curve based on the eqn (2):

$$\mu = [dI_{ds}/dV_g] \times [L/WC_gV_{ds}] \quad (2)$$

where C_g is the capacitance of the 300 nm thick SiO_2 layer. The mobility of $Mo_{0.84}W_{0.16}S_{1.64}Se_{0.36}$ is 1.9 cm^2 V^{-1} s^{-1}, which is similar to the value of CVD-grown monolayer $MoS_{2(1-x)}Se_{2x}$

FETs previously reported in the literature,[51] proving the high quality of the as-grown alloy. The output curve ($I_{ds} - V_{ds}$) of alloy FET displays a linear relationship (Fig. 7d), which indicates that the source and drain electrodes form typical ohmic contacts. Fig. 7e shows the transfer characteristic curve of monolayer $Mo_{0.18}W_{0.72}S_{0.40}Se_{1.60}$ FET measured at room temperature, since the monolayer WSe_2 is intrinsic p-type semiconductor, so the as-grown alloys exhibit bipolar conduction behavior with increasing W, Se content and on/off current ratio is significantly reduced. Meanwhile, the electron and hole field effect

mobilities are 0.64 and 0.25 cm^2 V^{-1} s^{-1} respectively. The mobility is dramatically deteriorated. The output curve ($I_{ds} - V_{ds}$) of alloy FET shows the perfect ohmic-type contact between sample and electrodes (Fig. 7f).

4. Conclusion

In this study, quaternary monolayer $Mo_xW_{(1-x)}S_{2y}Se_{2(1-y)}$ were successfully synthesized on sapphire substrates by using a robust liquid phase edge epitaxy (LPEE) method. This technique is a self-limiting growth process, leading exclusively to monolayer $Mo_xW_{(1-x)}S_{2y}Se_{2(1-y)}$.This synthetic approach achieves the compositionally tunable synthesis of quaternary monolayer $Mo_xW_{(1-x)}S_{2y}Se_{2(1-y)}$ with well-crystalled and thickness-controlled characteristics, as well as exhibits simplicity, safety, good reproducibility, and homogeneity. By adjusting the mass ratio of MoS_2/WSe_2 ($MoSe_2/WS_2$), monolayer $Mo_xW_{(1-x)}S_{2y}Se_{2(1-y)}$ with different atomic ratios were obtained. PL results indicate that the band gap can be continuously adjusted from WS_2 (1.55 eV) to $MoSe_2$ (1.99 eV) with a change in composition. Meanwhile, monolayer $Mo_xW_{(1-x)}S_{2y}Se_{2(1-y)}$ has exhibited a continuously broad spectrum, providing a new design idea for obtaining high-performance broad spectrum image sensors. Various characterization techniques exhibit good crystallinity and uniform distribution of components in the grown alloys. By adjusting the alloy composition, the carrier type and carrier mobility of alloy-based field-effect transistors can be systematically modulated. In particular, the adjustable conductivity of $Mo_xW_{(1-x)}S_{2y}Se_{2(1-y)}$ alloy from n-type to bipolar type is achieved for the first time. The LPEE method described in this study can regulate the atomic ratio of the synthesized materials by controlling the mass ratio of the growth source; in addition, the method has been proven suitable for designing the properties and functions of 2D monolayer materials. This approach can be used to synthesize more 2D semiconductor materials with potential applications in multifunctional electronic devices, catalysis, energy conversion, and spintronic devices.

Data availability

The data that support the findings of this study are available from the corresponding author upon reasonable request.

Author contributions

You Li: conceptualization, methodology, writing – original draft. Kangkang Wang: software. Junjie Qi and Liming Xie: project administration, supervision, funding acquisition. Yiwen Wang and Junyi Liao: data curation. Wenbin Huan: investigation. Ziyue Qian and Junqi Wang: visualization. Qichao Yang and Honggang Wang: writing – re-view & editing. Sabir Hussain: validation.

Conflicts of interest

The authors declare no conflict of interest.

References

1 J. M. Lu, O. Zheliuk, I. Leermakers, N. F. Yuan, U. Zeitler, K. T. Law and J. T. Ye, *Science*, 2015, **350**, 1353–1357.
2 L. Xu, L. Wang, H. Liu, F. Li, D. Li, Y. Cao, C. Wu, X. Bai and J. Qi, *J. Mater. Chem. C*, 2021, **9**, 5261–5266.
3 X. Wang, B. Wang, Q. Zhang, Y. Sun, E. Wang, H. Luo, Y. Wu, L. Gu, H. Li and K. Liu, *Adv. Mater.*, 2021, **33**, e2102435.
4 B. W. Su, X. L. Zhang, B. W. Yao, H. W. Guo, D. K. Li, X. D. Chen, Z. B. Liu and J. G. Tian, Laser Writable Multifunctional van der Waals Heterostructures, *Small*, 2020, **16**, e2003593.
5 J. Ye, W. Chen, Q. Chen, Z. Yu and J. Y. Lee, *Acta*, 2016, **190**, 538–547.
6 J. Hong, C. Wang, H. Liu, X. Ren, J. Chen, G. Wang, J. Jia, M. Xie, C. Jin, W. Ji, J. Yuan and Z. Zhang, *Nano Lett.*, 2017, **17**, 6653–6660.
7 P. K. Sahoo, S. Memaran, F. A. Nugera, Y. Xin, T. Díaz Márquez, Z. Lu, W. Zheng, N. Zhigadlo, D. Smirnov, L. Balicas and H. R. Gutiérrez, *ACS Nano*, 2019, **13**, 12372–12384.
8 S. Xie, M. Xu, T. Liang, G. Huang, S. Wang, G. Xue, N. Meng, Y. Xu, H. Chen, X. Ma and D. Yang, *Nanoscale*, 2016, **8**, 219–225.
9 C. Xie, L. Zeng, Z.-x. Zhang, Y. H. Tsang, L.-b. Luo and J. H. Lee, *Nanoscale*, 2018, **10**, 15285–15293.
10 K. L. Seyler, P. Rivera, H. Yu, N. P. Wilson, E. L. Ray, D. G. Mandrus, J. Yan, W. Yao and X. Xu, *Nature*, 2019, **567**, 66–70.
11 S. Fu, K. N. Kang, K. Shayan, A. Yoshimura, S. Dadras, X. Wang, L. Zhang, S. Chen, N. Liu, A. Jindal, X. Li, A. N. Pasupathy, A. N. Vamivakas, V. Meunier, S. Strauf and E. H. Yang, *Nat. Commun.*, 2020, **11**, 2034.
12 S. Y. Wang, T.-S. Ko, C. C. Huang, D.-Y. Lin and Y.-S. Huang, *Jpn. J. Appl. Phys.*, 2014, **53**, 04EH07.
13 Q. Li, X. Zhao, L. Deng, Z. Shi, S. Liu, Q. Wei, L. Zhang, Y. Cheng, L. Zhang, H. Lu, W. b. Gao, W. Huang, C.-w. Qiu, G. Xiang, S. J. Pennycook, Q. Xiong, K. P. Loh and B. Peng, *ACS Nano*, 2020, **14**, 4636–4645.
14 L. Yang, H. Wu, L. Zhang, G. Zhang, H. Li, W. Jin, W. Zhang and H. Chang, *ACS Appl. Mater. Interfaces*, 2021, **13**, 31880–31890.
15 X. Zhou, X. Hu, S. Zhou, H. Song, Q. Zhang, L. Pi, L. Li, H. Li, J. Lü and T. Zhai, *Adv. Mater.*, 2018, **30**, 1703286.
16 J. Zhang, W. Xie, J. Zhao and S. Zhang, *2D Mater*, 2017, **4**, 015038.
17 H. Henck, Z. Ben Aziza, D. Pierucci, F. Laourine, F. Reale, P. Palczynski, J. Chaste, M. G. Silly, F. Bertran, P. Le Fèvre, E. Lhuillier, T. Wakamura, C. Mattevi, J. E. Rault, M. Calandra and A. Ouerghi, *Phys. Rev. B*, 2018, **97**, 155421.

18 Z. Liu, A. Dibaji, D. Li, S. Mateti, J. Liu, F. Yan, C. J. Barrow, Y. I. Chen, K. Ariga and W. Yang, *Mater. Today*, 2021, **44**, 194.

19 F. Chen, S. Ding and W. Su, *J. Alloys Compd.*, 2019, **784**, 213.

20 A. G. Chanchal, *Matter*, 2006, **383**, 188–193.

21 A. Azizi, Y. Wang, G. Stone, A. L. Elías, Z. Lin, M. Terrones, V. H. Crespi and N. Alem, *Nano Lett.*, 2017, **175**, 2802–2808.

22 M. Zhang, J. Wu, Y. Zhu, D. Dumcenco, J. Hong, N. Mao, S. Deng, Y. Chen, Y. Yang, C. Jin, S. H. Chaki, Y.-S. Huang, J. Zhang and L. Xie, *ACS Nano*, 2014, **87**, 7130–7137.

23 H. Li, X. Duan, X. Wu, X. Zhuang, H. Zhou, Q. Zhang, X. Zhu, W. Hu, P. Ren, P. Guo, L. Ma, X. Fan, X. Wang, J. Xu, A. Pan and X. Duan, *J. Am. Chem. Soc.*, 2014, **10**, 3756–3759.

24 X. Duan, C. Wang, Z. Fan, G. Hao, L. Kou, U. Halim, H. Li, X. Wu, Y. Wang, J. Jiang, A. Pan, Y. Huang, R. Yu and X. Duan, *Nano Lett.*, 2016, **161**, 264–269.

25 S. Susarla, A. Kutana, J. A. Hachtel, V. Kochat, A. Apte, R. Vajtai, J. C. Idrobo, B. I. Yakobson, C. Tiwary and P. M. Ajayan, *Adv. Mater.*, 2017, **29**, 1702457.

26 Z. Wang, X. Zhao, Y. Yang, L. Qiao, L. Lv, Z. Chen, Z. Di, W. Ren, S. J. Pennycook, J. Zhou and Y. Gao, *Small*, 2020, **16**, e2000852.

27 S. Tongay, J. Zhou, C. Ataca, K. Lo, T. S. Matthews, J. Li, J. C. Grossman and J. Wu, *Nano Lett.*, 2012, **12**, 5576–5580.

28 Z. Liu, M. Amani, S. Najmaei, Q. Xu, X. Zou, W. Zhou, T. Yu, C. Qiu, A. G. Birdwell, F. Crowne, R. Vajtai, B. I. Yakobson, Z. Xia, M. Dubey, P. M. Ajayan and J. Lou, *Nat. Commun.*, 2014, **5**, 5246.

29 Y. Y. Hui, X. Liu, W. Jie, N. Y. Chan, J. Hao, Y. T. Hsu, L. J. Li, W. Guo and S. P. Lau, *ACS Nano*, 2013, **78**, 7126–7131.

30 S. B. Desai, G. Seol, J. S. Kang, H. Fang, C. Battaglia, R. Kapadia, J. W. Ager, J. Guo and A. Javey, *Nano Lett.*, 2014, **148**, 4592–4597.

31 T. M. G. Mohiuddin, A. Lombardo, R. R. Nair, A. Bonetti, G. Savini, R. Jalil, N. Bonini, D. M. Basko, C. Galiotis, N. Marzari, K. S. Novoselov, S. DUTTASINHA and A. C. Ferrari, *Phys. Rev. B*, 2009, **79**, 205433.

32 E. V. Castro, K. S. Novoselov, S. V. Morozov, N. M. R. Peres, J. L. L. dos Santos, J. Nilsson, F. Guinea, S. DUTTASINHA and A. H. C. Neto, *Phys. Rev. Lett.*, 2007, **99**, 216802.

33 E. V. Castro, K. S. Novoselov, S. V. Morozov, N. M. R. Peres, J. L. L. dos Santos, J. Nilsson, F. Guinea, S. DUTTASINHA and A. H. C. Neto, *Adv. Mater.*, 2014, **26**, 2648.

34 Q. Fu, L. Yang, W. Wang, A. Han, J. Y. Huang, P. Du, Z. Fan, J. Zhang and B. Xiang, *Adv. Mater.*, 2015, **27**, 4732.

35 F. Cui, Q. Feng, J. Hong, R. Wang, Y. Bai, X. Li, D. Liu, Y. Zhou, X. Liang, X. He, Z. Zhang, S. Liu, Z. Lei, Z. Liu, T. Zhai and H. Xu, *Adv. Mater.*, 2017, **29**, 1705015.

36 P. Tang, H. Shu, M. Yang, M. Zhang, C. Sheng, P. Liang, D. Cao and X. Chen, *ACS Appl. Nano Mater.*, 2021, **4**, 12609.

37 Q. Feng, N. Mao, J. Wu, H. Xu, C. Wang, J. Zhang and L. Xie, *ACS Nano*, 2015, **9**, 7450–7455.

38 K. Ding, Q. Fu, H. Nan, X. Gu, K. K. Ostrikov and S. Xiao, *Mater. Sci. Eng., B*, 2021, **269**, 115176.

39 S. Hussain, R. Zhou, Y. Li, Z. Qian, Z. Urooj, M. Younas, Z. Zhao, Q. Zhang, W. Dong, Y. Wu, X. Zhu, K. Wang, Y. Chen, L. Liu and L. Xie, *J. Am. Chem. Soc.*, 2023, **145**, 11348–11355.

40 J. Zhou, J. Lin, X. Huang, Y. Zhou, Y. Chen, J. Xia, H. Wang, Y. Xie, H. Yu, J. Lei, D. Wu, F. Liu, Q. Fu, Q. Zeng, C.-H. Hsu, C. Yang, L. Lu, T. Yu, Z. Shen, H. Lin, B. I. Yakobson, Q. Liu, K. Suenaga, G. Liu and Z. Liu, *Nature*, 2018, **556**, 355–359.

41 H. Wang, X. Huang, J. Lin, J. Cui, Y. Chen, C. Zhu, F. Liu, Q. Zeng, J. Zhou, P. Yu, X. Wang, H. He, S. H. Tsang, W. b. Gao, K. Suenaga, F. Ma, C. Yang, L. Lu, T. Yu, E. H. T. Teo, G. Liu and Z. Liu, *Nat. Commun.*, 2017, **8**, 394.

42 B. Jin, P. Huang, Q. Zhang, X. Zhou, X. Zhang, L. Li, J. Su, H. Li and T. Zhai, *Adv. Funct. Mater.*, 2018, **28**, 1800181.

43 M. Acerce, D. Voiry and M. Chhowalla, *Nat. Nanotechnol.*, 2015, **10**, 313–318.

44 D. Voiry, A. D. Mohite and M. Chhowalla, *Chem. Soc. Rev.*, 2015, **44**, 2702–2712.

45 Y. H. Lee, L. Yu, H. Wang, W. Fang, X. Ling, Y. Shi, C.-T. Lin, J.-K. Huang, M. T. Chang, C. S. Chang, M. S. Dresselhaus, T. Palacios, L. J. Li and J. Kong, *Nano Lett.*, 2013, **13**, 1852–1857.

46 H. Li, X. Wu, H. Liu, B. Zheng, Q. Zhang, X. Zhu, Z. Wei, X. Zhuang, H. Zhou, W. Tang, X. Duan and A. Pan, *ACS Nano*, 2017, **11**, 961–967.

47 M. B. Sreedhara, Y. Miroshnikov, K. Zheng, L. Houben, S. Hettler, R. Arenal, I. Pinkas, S. S. Sinha, I. E. Castelli and R. Tenne, *J. Am. Chem. Soc.*, 2022, **144**, 10530–10542.

48 J. P. Perdew, K. Burke and M. Ernzerhof, *Phys. Rev. Lett.*, 1996, **77**, 3865–3868.

49 G. Kresse and D. P. Joubert, *Phys. Rev. B*, 1999, **59**, 1758–1775.

50 Y. Zuo, C. Liu, L. Ding, R. Qiao, J. Tian, C. Liu, Q. Wang, G.-W. Xue, Y. You, Q. Guo, J. Wang, Y. Fu, L.-Y. D. Liu, X. Zhou, H. Hong, M. Wu, X. Lu, R. Yang, G. Zhang, D. Yu, E. Wang, X. Bai, F. Ding and K. Liu, *Nat. Commun.*, 2022, **13**, 1007.

51 R. Jenjeti, R. Kumar, K. Vankayala and S. Sampath, *J. Mater. Sci.*, 2022, **57**, 14339.